Supporting Information: Electrochemically Induced pH Change: Time-Resolved Confocal Fluorescence Microscopy Measurements and Comparison with Numerical Model

Nakul Pande,[*,†,‡] Shri K. Chandrasekar,[‡] Detlef Lohse,[†] Guido Mul,[‡] Jeffery A. Wood,[¶] Bastian T. Mei,[*,‡] and Dominik Krug[*,†]

†*Physics of Fluids, University of Twente, Enschede*
‡*Photo Catalytic Synthesis, University of Twente, Enschede*
¶*Soft Matter, Fluidics and Interfaces, University of Twente, Enschede*

E-mail: n.pande@utwente.nl; b.t.mei@utwente.nl; d.j.krug@utwente.nl

Experimental Methods

A Nikon inverted laser scanning confocal fluorescent microscope (Nikon confocal microscope A1 system, Nikon Corporation, Tokyo, Japan) with a 10x dry objective (CFI Plan Fluor 10x/0.3, numerical aperture = 0.3, working distance = 16 mm) was used in the resonant scanning mode (33 ms per image) to measure a 1.28 mm × 1.28 mm region (512 × 512 pixel^2) chosen close to the center of the electrode. A 488 nm excitation laser was chosen to excite Fl, while the emission was collected in a 515-550 nm wavelength window. The pinhole (29.4 μm) cuts off any out of focus light allowing to image thin volume sections. Close to 70 measurement cross sections with 20 μm distance from each other were scanned repeatedly , resulting in a total measured depth of 1.4 mm. The scanning along z proceeded from below the electrode surface into the solution and was repeated at a typical rate of 2 Hz. The acquisition frequency was limited by the movement of the stage in the z-direction. To determine the location of the electrode surface we measure the light reflection[1] from the working (glass slide) electrode. Figure 1 shows the mean reflection and fluorescein intensity signals measured simultaneously, starting from below the glass slide. The fluorescein signal does not provide clear information on the (electrode) surface location, hence the reflection signal is used. The presence of the glass slide causes two reflection maxima 115 μm apart, which can be used to establish the surface positions. Therefore, before starting each experiment, the reflection signal is measured (by scanning optical sections 5 μm apart) to determine where the surface of the electrode is located. It should be noted that even though a simplified Point Spread Function (PSF) has been assumed in the following analysis, the actual PSF will likely be more complicated due to the many different refractive index media (air-glass-chromium-platinum-water). While increasing the numerical aperture (NA) will increase the z-resolution[2] (z-resolution $\propto 1/\mathrm{NA}^2$), the choice was limited due to significant reduction in the measured fluorescent intensity signal at the electrode interface for high NA objectives as shown in Figure 1. This was likely due to the high refractive index contrast between the glass-metal interface, which at the large incident angles of a high NA objective, may cause considerable loss of trans-

mitted light due to internal reflection.

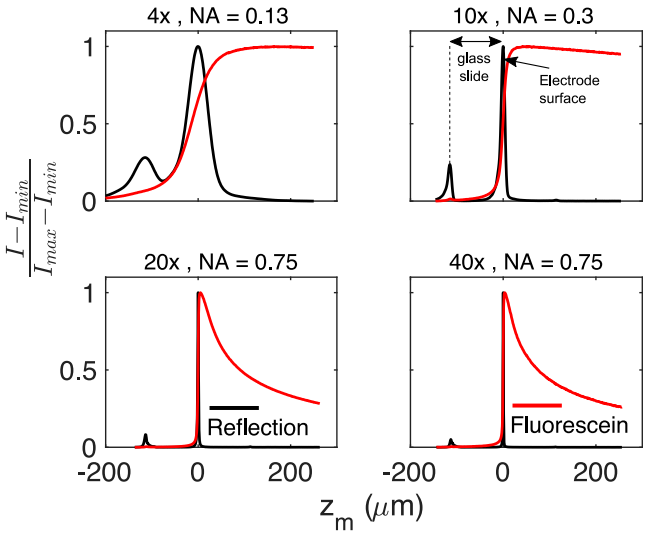

Figure 1: Surface reflection and fluorescein intensity for three different Numerical Apertures (NA's) and 4 different magnifications for a constant pH and Fluorescein concentration solution (E-cell off). Maxima in the surface reflection corresponds to the electrode surface.

In the experiments, sections in the scanned direction are taken by the programmed movement of the optical stage (20 μm apart in the experiments in the main text). The distances measured (z_m) in this way (from the electrode surface), however, do not take into account distortion in the light path due to variations in the refractive index (air vs. aqueous electrolyte). Visser and Oud[3] give the relationship between the actual focal distance (Δz) to stage movement (Δz_m) as $\Delta z = \Delta z_m n$, where n is the refractive index of the medium. To verify the appropriateness of this correction in our case, we consider the measured glass slide thickness of 115 μm (Δz_m). Using $n_{glass} = 1.5$, the corrected glass slide thickness then is $\Delta z = 115\ \mu\text{m} \times n_{glass} = 172.5\ \mu$m, very close to the actual value of 170 μm. We carry out a similar correction for the refractive index of the electrolyte solution (using $n_{sol} = 1.33$) such that $z = n_{sol} z_m$. So while the total measured depth is $z_m^{max} \approx 1.4$ mm, the corrected depth is $z^{max} \approx 1.9$ mm.

Any measurement of fluorescence requires considering the path dependent attenuation of the excitation as well as the emitted fluorescent light. Since the numerical aperture of the objective used in our experiments is small, following Ohser et al.,[9] the dependence of the emitted fluorescent light ($I_{em}(z)$) on the excitation intensity ($I_{ex}(z)$) and the concentration of fluorophore ($c(z)$) at a point z in the solution, along with the fluorescence efficiency (α_1, pH dependent in the case of Fluorescein) can be written as:

$$I_{em}(z) = I_{ex}(z)\alpha_1 c(z) \qquad \text{(s.1)}$$

Since in our case, the absorbance of the fluorophore is pH dependent,[8] and the pH itself is z dependent, the path dependent attenuation of the excitation intensity can be written as:

$$I_{ex}(z) = I_{ex0}\left(e^{-\int_0^z \epsilon_1(pH(\tau))c(\tau)d\tau}\right) \qquad \text{(s.2)}$$

where ϵ_1 is the pH dependent attenuation coefficient of the excitation light and I_{ex0} is the excitation intensity at $z = 0$. Similarly if there is an attenuation (ϵ_2) of the emitted light $I_{em}(z)$, the measured fluorescence intensity $I_f(z)$ goes as:

$$I_f(z) = I_{em}(z)\left(e^{-\int_z^0 \epsilon_2(pH(\tau))c(\tau)(-d\tau)}\right) \qquad \text{(s.3)}$$

Since we use a constant concentration of fluorophore and laser settings in all our experiments, combining equations (s.1), (s.2) and (s.3):

$$I_f(z) = I_{f0}\left(e^{-\int_0^z k(pH(\tau))d\tau}\right) \qquad \text{(s.4)}$$

where $I_{f0} = \alpha_1 I_{ex0} c$ is the unattenuated fluorescence intensity, and $k = (\epsilon_1 + \epsilon_2)c$ is the overall attenuation factor. Hence a optical path history dependent correction factor of $e^{\int_0^z k(pH(\tau))d\tau}$ must be multiplied with the fluorescence intensity, $I_f(z)$, measured at a point to get the corresponding corrected value I_{f0}. It should be noted that for higher numerical aperture objectives, an attenuation correction such as shown in Visser and Oud[10] must be used.

To determine k, we measured the fluorescence intensity as a function of z for different constant pH solutions (k is constant for a constant pH) similar to that shown in Figure 2a. We expect the fluorescence intensity at a particular pH to

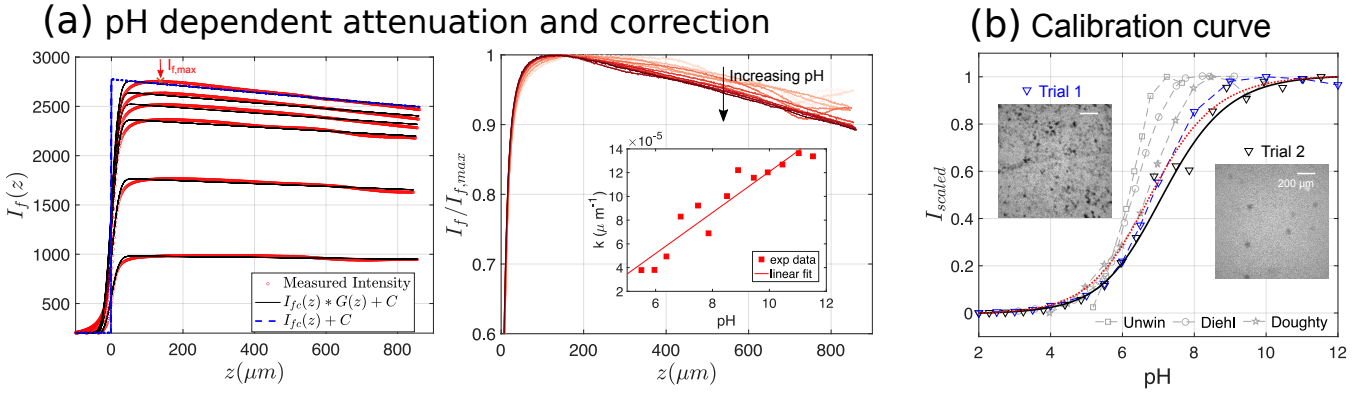

Figure 2: (a) Left: fluorescein intensity values (average over 3 runs) obtained for different pH shown by the red markers (pH ≈ 7.5-11.5 in steps of 1). Black line shows corresponding fit. Blue line shows the simplified fit with the obtained attenuation coefficients. Right: Normalized intensity (with their respective maximum) showing attenuation at high pH. Inset: the exponential coefficients as a function of pH. The linear fit is described by: $k = (1.7 \times pH - 5.2) \times 10^{-5}$ μm^{-1}. (b) Comparison of Intensity-pH relationship of Fluorescein obtained by different authors: Unwin[4,5] , Doughty[6] , Diehl[7] against two trials measured for this study. The solid line shows the sigmoidal fit in equation (s.8), similarly scaled. The dotted red line represents the same fit adjusted to an ionic strength corresponding to 0.5 M of a monovalent salt following Sjöback et al..[8] The dashed lines have been added for better visibility of markers.

be exponentially decaying step function ($I_{fc}(z)$ given by equation (s.4) with $k = \text{const}$) and its maximum at the electrode surface, $z = 0$. The actual profiles, however, are smooth close to the electrode surface, most likely due to the point spread function (psf in the z direction) of the optical system. Taking the simplest assumption of a gaussian psf i.e. $G(z) = \frac{1}{\sigma\sqrt{2\pi}} e^{-\frac{z^2}{2\sigma^2}}$ (with the standard deviation σ), the resulting profiles must then be a convolution of $I_{fc}(z)$ with $G(z)$, and should have the analytical form:

$$I_{fc}(z) * G(z) = I_{f0} e^{-kz} e^{\frac{\sigma^2 k^2}{2}} \left(1 - \frac{1}{2} erfc\left(\frac{z}{\sigma\sqrt{2}} - \frac{k\sigma}{\sqrt{2}}\right)\right) \quad \text{(s.5)}$$

where, $erfc$ is the complementary error function. Consequently, we fit a function of the form $I_{fc}(z) * G(z) + C$, with four fitting parameters I_{f0}, k, σ and C (where C is a parameter related to small constant unknown effects). The resulting fit is overlaid on the original data of constant pH solutions (average of 3 measurements) in fig 2a. The fit is reasonable, however differences in the location of their maximum indicates that the psf is likely more complicated than a gaussian function. Based on the I_{f0} and k and C obtained, we further plot $I_{fc}(z) + C$ which shows that the psf smoothening is important only at the electrode surface. In our measurements, we therefore correct only for this attenuation and not the psf smoothening. The measurement is compromised below the location of the intensity maximum ($I_{f,max}$ in Figure 2a) of the profiles (≈ 100 μm) and has not been shown in the main text. The attenuation correction factor k as a function of pH is plotted in the inset of figure, and has been fitted with a line. At the n-th stack from the electrode surface (with a distance $\Delta z = 20 \times 1.33$ μm), the measured fluorescein intensity then must be of the form:

$$I_f(z) = I_{f0} e^{-\sum_{\eta=0}^{n-1} k(pH(\eta))\Delta z} + C \quad \text{(s.6)}$$

The unattenuated fluorescein intensity ($I_{f,org}$, which is now $I_{f,org} = I_{f0} + C$) can now be calculated based on the k and C and is:

$$I_{f,org} = (I_f(z) - C) e^{\sum_{\eta=0}^{n-1} k(pH(\eta))\Delta z} + C \quad \text{(s.7)}$$

Lastly, it should be noted that the correction

in equation (s.7) obtained (using k and C) is calculated at each position based on the uncorrected pH. However any error associated with this is expected to be minimal.

Figure 2b compares the intensity variation of Fluorescein emission with pH measured by the authors to corresponding results in literature. For our calibration, the maximum of the fluorescence intensity measured along the scanned direction ($I_{f,max}$ in Figure 2a), for different constant pH solutions is taken as the reference intensity. The intensity variation with pH (as shown in Figure 5b in the main text), obtained so, is rescaled to the range from 0 to 1, to render the data comparable with literature results (which were similarly rescaled where needed). The general trend matches in all cases, however, there is significant spread especially at the upper limit of the pH-sensitive region. The different ionic strengths of the calibration solution could be a possible reason for these differences.[8] However, this effect is small as the red dotted line, which represents our calibration curve corrected to an ionic concentration of a 0.5 M monovalent salt (using the equation in Sjöback et al.;[8] assuming that the parameter γ in our fit behaves like an effective pKa), in Figure 2c shows. Moreover, since the fluorescence intensity at a point in the sample is related to the the local concentration of the fluorophore, the laser excitation intensity, the optical path history of the light, the voltage of the photo-multiplier tube etc., the differences could be due to a number of reasons and it is not straightforward to compare the values of fluorescence intensity, for different pH, across optical setups. Rather, laser and camera settings must remain constant between calibration and experiment for a faithful conversion of intensity values to pH. Even then, there are small differences between the repeats of our calibration measurements (new pH solutions and different electrode) in Figure 2a and these could be traced to presence of small contaminants on the electrode surface. The inset of Figure 2a shows an example of a fluorescein intensity image (at pH = 10) obtained for each of the two calibration trials done. The difference between the repeats provides a sense of the calibration error as similar (and to varying degrees) contamination could be present in the experiments. However, since the calibration curve is similar in the lower limit of the pH-sensitive region, the effect on the location of the pH shoulder is minimal. Still, trial 2 (having the cleaner electrode) is used in our measurements and is shown Figure 5b in the main text. Lastly, the intensity dependence on pH (in Figure 5b in the main text) is fit with a function of the form

$$\ln(I_{f,max}) = \alpha + \frac{\beta}{1 + e^{-(pH-\gamma)}} \qquad \text{(s.8)}$$

with fit parameters α (4.991±0.034), β (2.946± 0.039) and γ (5.857 ± 0.060). A robust least-squares regression with a logistic function weight (implemented as 'nlinfit' in MATLAB) is used for fitting the data. The residuals of the regression appeared to be normally distributed (at all points except the two measurement triplicates between pH 6 and 8 that are not on the line in Figure 5b). The inverse function is therefore:

$$pH_{inv} = -\ln\left(\frac{\beta}{\ln(I_{f,max}) - \alpha} - 1\right) + \gamma. \qquad \text{(s.9)}$$

The prediction interval for the non-linear

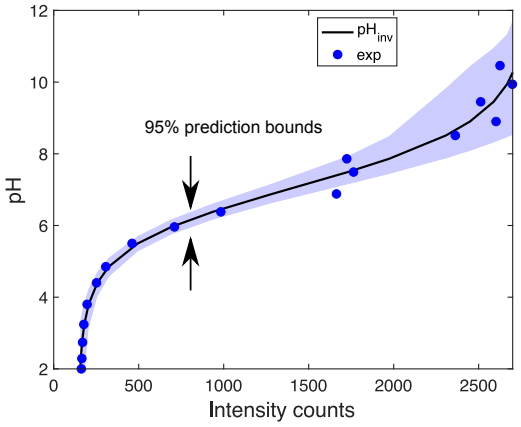

Figure 3: The inverse function based on calibration measurements presented in the main text. At a given pH, the mean of three separate intensity measurements is shown here, since the error bars are small.

fit (based on the measured calibration data) presented in Figure 3 is calculated based on Guthrie et al.[11] and shows that at the higher

ends of our pH-sensitive range, the error in measurement can be close to ±1 pH unit.

All remaining fits presented here use the 'fit' function in Matlab (R2019b).

Dye migration effects: limits to supporting electrolyte concentration

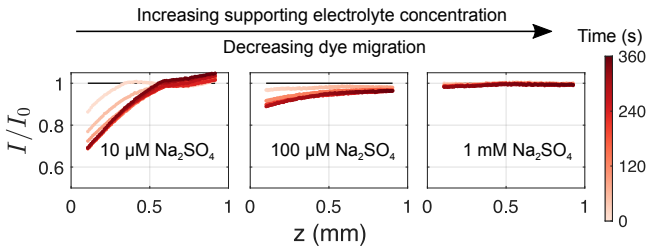

Figure 4: Migration effect for different supporting electrolyte concentrations. The emission intensity (I) is normalized with the intensity profile before applying the current (I_0). The measurement of fluorescence intensity is restricted to $z > 0.1$ mm due to limitations of the optical setup (see supporting information for details) . The measurements were performed with a solution containing 8μM SRb. pH was adjusted to pH 5 by addition of H_2SO_4. The color code reflects the time at which the concentrations were measured. $|i| = 5.59\ \mu A/cm^2$.

Since Fl is charged in solution, an electric field induced inhomogeneity in the dye distribution will make it difficult to decouple intensity changes due to migration from a pH change. An anionic[12] pH insensitive dye, namely Sulforhodamine B (Sigma Aldrich, Molecular weight: 580.65 g/mol, 8μM, henceforth SRb) was therefore used to indicate the presence of dye migration. Although unlike Fl, SRb has a single negative charge in solution, due to their similar molecular weight it still serves as a good qualitative indicator of dye migration. SRb is also mildly temperature sensitive (intensity decrease $\approx 1.2\%$ per K[13]), but for the current densities considered in this work the temperature change is estimated (even when using resistivity of pure water) to be negligible. The measured fluorescent intensity for the highest current density ($5.59\ \mu A/cm^2$) in this work is presented in Figure 4c. For low supporting electrolyte concentration, i.e. $= 10\ \mu$M, the fluorescence intensity of the dye near the electrode surface and up to a distance of ≈ 0.75 mm above the electrode decreased by up to 30 %. However, this migration effect reduces significantly for increased concentration of the supporting electrolyte, and is almost negligible for Na_2SO_4 concentrations $\geq$ 1mM. A concentration of the supporting electrolyte much greater than this is therefore used in the experiments performed in this study.

Details of the numerical model

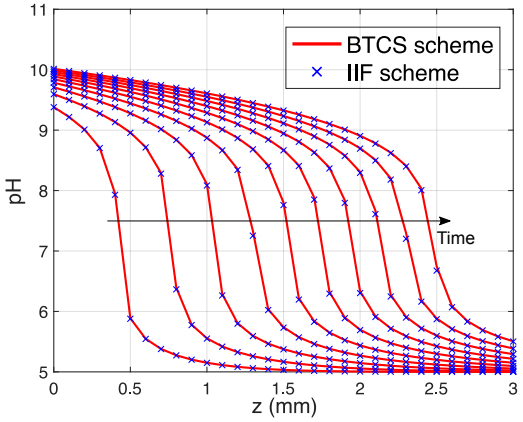

Figure 5: Comparison of results using BTCS and IIF numerical schemes. Note: only the H^+ and OH^- ions were considered for this comparison. The relatively small effect of HFl^- on the pH profiles is consequently also absent.

For each ion species k, we have a related non-dimensionalized concentration diffusion equation of the type shown in equation (1) in the main text. Assuming that the concentration of water is large and therefore essentially constant during the experiment the differential equations

simplify to:

$$\frac{\partial c^*_{H^+}}{\partial t^*} = \frac{\partial^2 c^*_{H^+}}{\partial z^{*2}} - Da_1(c^*_{H^+}\ c^*_{OH^-} - 1) - Da_2\left(c^*_{H^+}\ c^*_{Fl^{2-}} - \frac{K_{f,eq}}{c^0_{H^+}}(1 - c^*_{Fl^{2-}})\right) \tag{s.10a}$$

$$\frac{\partial c^*_{OH^-}}{\partial t^*} = D_{r,1}\ \frac{\partial^2 c^*_{OH^-}}{\partial z^{*2}} - \frac{Da_1 c^0_{H+}}{c^0_{OH^-}}(c^*_{H^+}\ c^*_{OH^-} - 1) \tag{s.10b}$$

$$\frac{\partial c^*_{Fl^{2-}}}{\partial t^*} = D_{r,2}\ \frac{\partial^2 c^*_{Fl^-}}{\partial z^{*2}} - \frac{Da_2 c^0_{H+}}{T}\left(c^*_{H^+}\ c^*_{Fl^{2-}} - \frac{K_{f,eq}}{c^0_{H^+}}(1 - c^*_{Fl^{2-}})\right) \tag{s.10c}$$

where,

$$Da_1 = \frac{k_f c^0_{OH^-} L^2}{D_{H^+}}, \quad Da_2 = \frac{k_{f,Fl} T L^2}{D_{H^+}}, \quad D_{r,1} = \frac{D_{OH^-}}{D_{H^+}}, \quad D_{r,2} = \frac{D_{Fl^{2-}}}{D_{H^+}}.$$

Further T is the total initial concentration of fluorescein ($c_{HFl^-} + c_{Fl^{2-}}$) which is used to non-dimensionalize the diffusion equation for $c_{Fl^{2-}}$.

All concentrations are kept constant far from the electrode ($z = L$) at their respective initial values, while flux boundary conditions are employed at the electrode surface. In particular, the consumption flux of H^+ is set by the Faradaic current density i_f as $\frac{\partial c^*_{H^+}}{\partial z^*} = \frac{-|i_f|L}{F D_{H^+} c^0_{H^+}}$, with F denoting the Faraday constant, while all other fluxes are zero at $z = 0$. It is important to note that i_f is not the applied current density i, but has been modified to take the contribution of a capacitive current into account. This is achieved by using a constant capacitance similarly as done by Bonnefont et al..[14] Assuming a Stern layer thickness $\lambda_S = 1$nm, a permittivity 10 times the vaccum permittivity[15] ϵ_0, and that the whole potential drop occurs within the Stern layer, the capacitance C is estimated to be about $C \approx 88\ \mu$F/cm^2. The double layer capacitance of platinum (measured in 0.1 M $KClO_4$) was found to be in a similar range (20 - 120 μF/cm^2).[16] i_f is then related to the measured time-dependent potential (ϕ) change by $i_f = i - C\frac{d\phi}{dt}$. Since the exact value of C in our measurements is not known, results for $0 \le C \le 120\ \mu$F/cm^2 have also been presented in Figure 3c in the main text.

Table 1: Parameters and associated used in the model

Parameter	Value (units)	Parameter	Value (units)
D_{H^+}	$9.3 \times 10^{-9}\ (m^2/s)^5$	T	$8 \times 10^{-6}\ (M)$
D_{OH^-}	$4.62 \times 10^{-9}\ (m^2/s)^5$	$k_{f,Fl}$	k_f
$D_{Fl^{2-}}$	$0.42 \times 10^{-9}\ (m^2/s)^{17}$	$K_{f_{eq}}$	$4.36 \times 10^{-7}\ (M^{-1})^7$
k_f	$1.4 \times 10^{11}\ (M^{-1}s^{-1})^{18}$	Area	$4\pi \times 10^{-4}\ (m^2)$
k_b	$2.6 \times 10^{-5}\ (s^{-1})^{18}$	$C_S = 10\epsilon_0/\lambda_s$	88 (μF/cm^2)[14]

The large reaction rate constants and the associated large Damköhler numbers ($Da \gtrapprox 10^6$) render the system of equations very stiff. To nonetheless numerically handle them efficiently, an implicit integrating factor formulation was adopted.[19,20]

A second order central difference scheme is used to discretize spatial gradients. The numerical domain of length L is divided into $N+1$ grid points such that $\Delta z = \frac{L}{N}$. We then obtain a set of equations of the form:

$$\frac{\partial \boldsymbol{c^*_k}}{\partial t^*} = \frac{D_{r,k}}{\Delta z^2}\left(\begin{bmatrix} -2 & 2 & 0\cdots & \\ 1 & -2 & 1 & \cdots \\ \vdots & \vdots & \ddots & \vdots \\ 0 & \cdots & 1 & -2 \end{bmatrix} \begin{bmatrix} c^*_k(1) \\ \vdots \\ c^*_k(N) \end{bmatrix} + \begin{bmatrix} \pm J_k \Delta z \\ 0 \\ \vdots \\ \\ c^*_k(N+1) \end{bmatrix}\right) \pm Da \times f(\boldsymbol{c^*}) \tag{s.11}$$

Here $\boldsymbol{c^*_k} = c_k(m)$ is the (non-dimensional) spatially discretized concentration ($1 \le m \le N+1$, but continuous in time) of ions and J_k is the constant flux of the ions at the electrode surface. In our simulations:

$$c^*_{H^+}(N+1) = 1 \tag{s.12a}$$

$$c^*_{OH^-}(N+1) = 1 \tag{s.12b}$$

$$c^*_{Fl^{2-}}(N+1) = \frac{c_{Fl^{2-}}}{T} \tag{s.12c}$$

and,

$$J_{H^+} = \begin{cases} 0, & \text{if } |i_{Cap}| > |i| \\ \frac{(-|i|+|i_{Cap}|)L}{FD_{H^+}c^0_{H^+}}, & \text{otherwise} \end{cases} \quad \text{(s.13a)}$$

$$J_{OH^-} = 0 \quad \text{(s.13b)}$$

$$J_{Fl^{2-}} = 0 \quad \text{(s.13c)}$$

where i_{Cap} is the time dependent capacitive current density as described in the main text.

The above set of equations are stiff due to large reaction rate constants (and related Da) for the non-linear reaction terms $f(c)$. Using an implicit scheme such as Backward-Time-Central-Space (BTCS), would therefore require very small time steps and consequently a large run-time. We instead integrate in time according to the implicit integrating factor (IIF) scheme presented in Nie et al..[19] A second order approximation of the $f(c)$-term is used, while employing the trapezoid rule to approximate the integration of the time dependent i_{Cap}. The set of non-linear equations are then solved at each time step using the *fsolve* function in Matlab (R2019b). The numerical scheme was validated, first with the analytical solution of the linear reaction-diffusion equation used in Nie et al..[19] We further compared the results of the IIF with the BTCS scheme (for our system) for the highest current density used in this work ($|i| = 5.59$ μA/cm^2). The results compare well as shown in Figure 5, confirming the proper implementation of the numerical scheme.

Repeat experiments

Figure shows the measured pH profiles in a repeated experiment has been provided to highlight the reliability of the measurement method. A comparison of the pH front with the model results is also shown. Similar to the results presented in the main text, the experimental profiles are in good agreement at the two lower current densities and deviate from the 1D diffusion model at the two highest current densities.

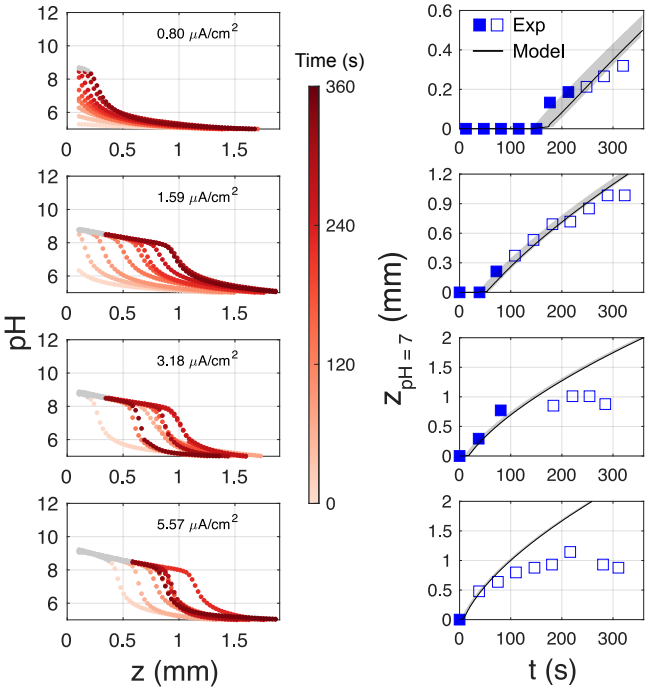

Figure 6: Experimental repeats for all $|i|$ presented in the main text. Left: pH profile measured. pH > 8.5 has been grayed out due to the uncertainty in measurement described in the main text. Right: Comparison of depletion length, $z_{pH=7}$, of experiment versus model. The shaded region indicates the model results over a range of capacitance $0 \leq C \leq 120$ μF/cm^2 (solid line with C $= 88$ μF/cm^2). Open squares show pH front after the first appearance of inhomogeneity described in the main text.

Sulfates comparison

To account for the buffering capacity of sulfates (Na_2SO_4/H_2SO_4) we adjusted the model to include the following reaction couples:

$$H^+ + {SO_4}^{2-} \underset{k_{f,S}}{\overset{k_{b,S}}{\rightleftharpoons}} {HSO_4}^- \qquad \text{(s.14)}$$

$$Na^+ + {SO_4}^{2-} \underset{k_{f,Na}}{\overset{k_{b,Na}}{\rightleftharpoons}} {NaSO_4}^- \qquad \text{(s.15)}$$

There is an extra bulk reaction term due to ${HSO_4}^-$ ionization in the H^+ equation. Furthermore, additional reaction diffusion equations (${SO_4}^{2-}$ and ${NaSO_4}^-$ here) and have to be taken into account. The initial concentrations of the ions are estimated based on the total dissolved Na_2SO_4 and pH of the solution. The dissociation constants of ${HSO_4}^-$ [21–23] and ${NaSO_4}^-$ [24,25] are taken from the literature ($K_{HSO4} = 0.0103$ and $K_{NaSO4} = 0.5$). Also for the forward rate constants $k_{f,Na} = k_f \times 0.1$ and $k_{f,S}$ [26] $= k_f \times 5$ are taken.

Figure 7 shows a comparison of the full pH profiles for the 4 different current densities considered. The buffer effect at the two lower current densities is captured well by the model, although the profiles do not match exactly at all times. Finally, the two highest current densities have been presented here only for the sake of completeness, as (discussed in the main text) experiments at these values of $|i|$ are marked by the appearance of inhomogeneous fluorescein intensity in a plane and therefore do not follow a 1D diffusion approximation.

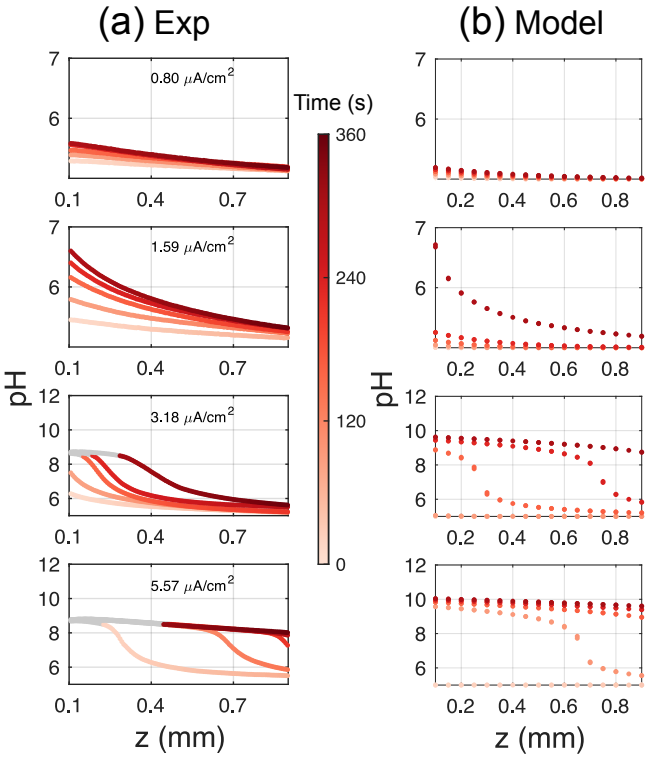

Figure 7: pH versus Depth for the case with sulfates: Experiments versus Simulations. (a) The experimental profiles for all $|i|$ values. (b) Numerical pH profiles based on values discussed in the text.

References

(1) Paddock, S. Confocal Reflection Microscopy: The "Other" Confocal Mode. *BioImaging* **2002**, *32*, 274–277.

(2) Claxton, N. S.; Fellers, T. J.; Davidson, M. W. *Encycl. Med. Devices Instrum.*; John Wiley & Sons, Inc.: Hoboken, NJ, USA, 2006.

(3) Visser, T. D.; Oud, J. L. Volume measurements in three-dimensional microscopy. *Scanning* **2008**, *16*, 198–200.

(4) Cannan, S.; Douglas Macklam, I.; Unwin, P. R. Three-dimensional imaging of proton gradients at microelectrode surfaces using confocal laser scanning microscopy. *Electrochem. commun.* **2002**, *4*, 886–892.

(5) Rudd, N. C.; Cannan, S.; Bitziou, E.; Ciani, I.; Whitworth, A. L.; Unwin, P. R. Fluorescence Confocal Laser Scanning Microscopy as a Probe of pH Gradients in Electrode Reactions and Surface Activity. *Anal. Chem.* **2005**, *77*, 6205–6217.

(6) Doughty, M. J. pH dependent spectral properties of sodium fluorescein ophthalmic solutions revisited. *Ophthalmic Physiol. Opt.* **2010**, *30*, 167–174.

(7) Diehl, H.; Markuszewski, R. Studies on fluorescein—VII: The fluorescence of fluorescein as a function of pH. *Talanta* **1989**, *36*, 416–418.

(8) Sjöback, R.; Nygren, J.; Kubista, M. Absorption and fluorescence properties of fluorescein. *Spectrochim. Acta Part A Mol. Biomol. Spectrosc.* **1995**, *51*, L7–L21.

(9) Ohser, J.; Haas, P.; Farbach, F.; Menstell, P.; Schwämmle, A.; S., O.; Dobrovolskij, D. Attenuation correction for confocal laser scanning microscopy and its application in chromatography. *J. Microsc.* **2020**, *00*, jmi.12888.

(10) Visser, T. D.; Groen, F. C.; Brakenhoff, G. J. Absorption and scattering correction in fluorescence confocal microscopy. *J. Microsc.* **1991**, *163*, 189–200.

(11) Guthrie, W.; Filliben, J.; Heckert, A. In *NIST/SEMATECH e-Handbook of Statistical Methods*; Guthrie, W., Ed.; 2020.

(12) Suzuki, T.; Sato, T.; Zhang, J.; Kanao, M.; Higuchi, M.; Maki, H. Electrochemically switchable photoluminescence of an anionic dye in a cationic metallo-supramolecular polymer. *J. Mater. Chem. C* **2016**, *4*, 1594–1598.

(13) Coppeta, J.; Rogers, C. Dual emission laser induced fluorescence for direct planar scalar behavior measurements. *Exp. Fluids* **1998**, *25*, 1–15.

(14) Bonnefont, A.; Argoul, F.; Bazant, M. Z. Analysis of diffuse-layer effects on time-dependent interfacial kinetics. *J. Electroanal. Chem.* **2001**, *500*, 52–61.

(15) Retter, U. Electrified Interfaces in Physics, Chemistry and Biology. *Zeitschrift für Phys. Chemie* **1992**, *177*, 120–121.

(16) Pajkossy, T.; Kolb, D. Double layer capacitance of Pt(111) single crystal electrodes. *Electrochim. Acta* **2001**, *46*, 3063–3071.

(17) Casalini, T.; Salvalaglio, M.; Perale, G.; Masi, M.; Cavallotti, C. Diffusion and Aggregation of Sodium Fluorescein in Aqueous Solutions. *J. Phys. Chem. B* **2011**, *115*, 12896–12904.

(18) Stillinger, F. H. *Theor. Chem. Adv. Perspect.*; 1978; Vol. 3; pp 177–234.

(19) Nie, Q.; Zhang, Y.-T.; Zhao, R. Efficient semi-implicit schemes for stiff systems. *J. Comput. Phys.* **2006**, *214*, 521–537.

(20) Chou, C. S.; Zhang, Y. T.; Zhao, R.; Nie, Q. Numerical methods for stiff reaction-diffusion systems. *Discret. Contin. Dyn. Syst. - Ser. B* **2007**, *7*, 515–525.

(21) Hamer, W. J. The Ionization Constant and Heat of Ionization of the Bisulfate Ion from Electromotive Force Measurements 1. *J. Am. Chem. Soc.* **1934**, *56*, 860–864.

(22) Covington, A. K.; Dobson, J. V.; Wynne-Jones, L. Dissociation constant of the bisulphate ion at 25°C. *Trans. Faraday Soc.* **1965**, *61*, 2057–2062.

(23) Wu, Y. C.; Feng, D. The second dissociation constant of sulfuric acid at various temperatures by the conductometric method. *J. Solution Chem.* **1995**, *24*, 133–144.

(24) Pytkowicz, R. M.; Kester, D. R. Harned's rule behavior of NaCl-Na_2SO_4 solutions explained by an ion association model. *Am. J. Sci.* **1969**, *267*, 217–229.

(25) Santos, M. M.; de Guedes, J. R. F.; Carvalho,; Guedes de Carvalho, R. A. Determination of the association constant of $NaSO_4^-$ with the sodium-selective electrode. *J. Solution Chem.* **1975**, *4*, 25–29.

(26) Irish, D. E.; Chen, H. Equilibria and proton transfer in the bisulfate-sulfate system. *J. Phys. Chem.* **1970**, *74*, 3796–3801.